Effects Of Engine Nacelle Dimension On Steam Turbine Cooling Performance And Optimization Of Dimension To Improve Cooling Performance

Sajad Rastad [1], Seyed Amir Abbas Oloomi [1]*, Seyed Ali Agha Mirjalily [1], Abolfazl Zare-Shahabadi [2]

[1]Department of Mechanical Engineering, Ya.C., Islamic Azad University, Yazd, Iran
[2]Department of Mechanical Engineering, National University of Skills (NUS), Tehran, Iran
* Corresponding author; Seyed Amir Abbas Oloomi Email: Amiroloomi@iau.ac.ir

Abstract
Considering the importance of increasing the performance of steam turbines and the effect of dimensional optimization on them, this paper aims to investigate the impacts of the nozzle's optimum axial distance to the engine nacelle and the engine nacelle length on the engine's performance. In order to provide a close simulation of the actual condition, the results were obtained by solving the 2D steady-state compressible Reynolds-averaged Navier-Stokes (RANS) equations using the Finite Volume Method and the Shear Stress Transport (SST) turbulence model (FVM). The findings demonstrated that the mass flow rate of the coolant fluid rose by more than 50% as the nacelle length increased but was not considered when the nozzle-to-nacelle distance increased.

Keywords: Finite Volume Method, SST (K-ω) model, Nozzle design, Engine nacelle length, Coolant rate.

1- Introduction

A steam turbine could be a machine that extricates warm vitality from pressurized steam and employments it to perform mechanical work on a turning yield shaft. Its modern expression was created by Charles Parsons in 1884. Modern steam turbine manufacturing requires advanced metalworking, forming high-quality alloy steel into precision components using techniques first attainable in the 20th century. Continued approach in steam turbine durability and capability continue to be central to the 21st century power industry. Steam turbines are a type of heat engine, and most of the advancement in thermodynamic efficiency comes from using multiple point to expand the steam, closer to the optimal reversible expansion action,[1-5]. Turbines produce rotational motion, so they can be coupled to generators to convert that motion into electricity. Such turbogenerators are the heart of thermal power plants powered by fossil, nuclear, geothermal or solar energy. About 85% of all US electricity production in 2014 was achieved using steam turbines [6-11]. The nacelle is nothing more than an aircraft engine housing to defend the gas turbine from derived object ingestion (FOI). Designed to efficiently feed the fan with minimal distortion and enlarged the gases in the exhaust mechanism with maximum utility. A nacelle is "a streamlined body sized for its contents," much like an airplane engine, fuel, or equipment. When attached to a pylon completely outside the airframe, it is sometimes called a pod. In this case they are mounted with pylons or struts and the thrusters are called pod thrusters. In some cases, such as the typical WWII-era Furman "Pusher" aircraft and his P-38 Lightning, the aircraft's cockpit is housed in the nacelle rather than the traditional fuselage. Multi-engine aircraft typically use nacelles to house the engines. In fighter aircraft (such as the Eurofighter Typhoon) the engine is frequently mounted in the fuselage. Some motor are built into the wings of the aircraft, such as the de Havilland Comet and Flying Wing jet. The engines can be in individual nacelles, or in larger aircraft such as the Boeing B-52 Stratofortress (pictured right), he can have two engines in one nacelle. Nacelles can be fully or partially removable to hold consumables such as fuel and weapons. Nacelles can be used to house equipment that functions only away from the fuselage. For example, the Boeing E-3 Sentry Radar is housed in a nacelle called a radome [12-20].

ANSYS Fluent was used in the current study to simulate computational fluid dynamics (CFD) [21-26]. By performing a numerical analysis and designing a nozzle, it was possible to investigate the pressure and temperature distribution inside the nozzle shape and to determine the thermal loads present at each location. Using input parameters from a thermochemical equilibrium analysis software program used to design the nozzle, temperature and pressure conditions at the inlet were determined. The model was run in an atmospheric environment. After obtaining the required outlines, axisymmetric two-dimensional modeling was carried out. The structural study conducted using ANSYS to choose the right throat insert material used the analysis presented in the current paper as its input and beginning component. The findings indicate that lengthening the nacelle boosts the coolant fluid's mass flow rate by 50%.

2-Modeling and Simulation

2.1 Numerical Method

The problem includes a steady flow of compressible fluid using a divergent, convergent nozzle with specific geometry, as shown in Fig.1, where D1=10mm, D2=25mm, L=350mm and H=100mm. The numerical modeling and analysis were used to solve the RANS equations in the flow field. The numerical computations of flow fluid were performed using ANSYS Fluent. The two-equation Menter's Shear Stress Transport (SST k-ω) model [22] was used as a turbulence model to appropriately calculate the complicated adverse pressure-gradient flows, separation flows, and the closed equations system with the ideal gas equation of state, k-ω SST, is a widely used and robust two-equation eddy-viscosity turbulence model used in Computational Fluid Dynamics(CFD). The model combines the k-ω and K-ε turbulence model such that the k-ω is used in the inner region of the boundary layer and switches to the K-ε in the free shear flow. A finite volume method is applied [23-25]. The mass imbalance is less than 0.001%, and the turbulent intensity is 5%.

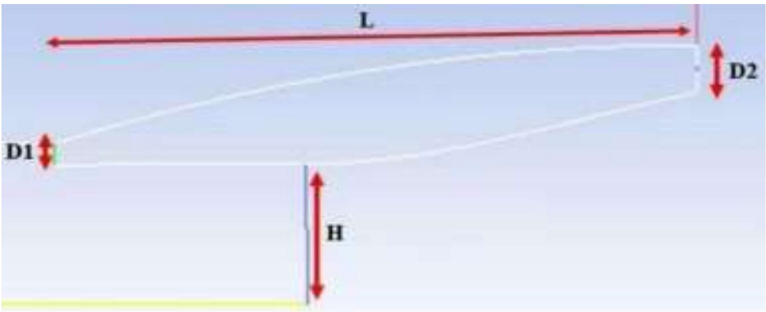

Fig.1The geometry problems

The density-based solver in ANSYS FLUENT was used along with the implicit formulation. For all variables, the second-order discretization was set up. The ideal gas equation was used to model density variation. Fig.2 illustrates the 2D structured mesh of the original design of the nacelle and nozzle of the engine. Applying the multi-block technique in Gambit, the mesh was generated. The viscosity-affected near-wall region was resolved, and Y^+ was made less than one for the cell next to the wall. To ensure $Y^+1\sim$ on the nozzle boundary, the height of the first cell on the nozzle was set to 0.000005 m. This value of the first cell height can be used to accurately represent the boundary layer flow mechanics at engine output. A fine mesh was created in this area as a result of the wake and flow separation that was present close to the engine output.

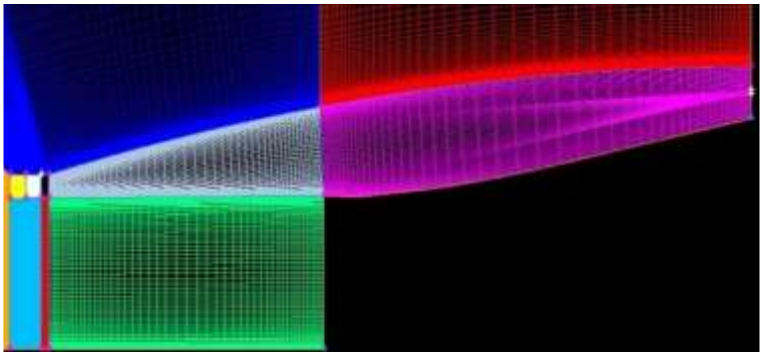

Fig.2 Original mesh of the nacelle and nozzle of the engine.

The flow direction’s outlet temperature in the engine is 1053K. Only half of the geometry has been computed because of axial symmetry. At the outlet of the nozzle, the boundary condition of Mass Flow Inlet is used also Pressure Inlet boundary condition has used for air holes. All dimensions, velocities, temperatures are dimensionless. All walls are considered smooth and no-slip condition is used in them. The imposing axisymmetric condition also decreases the computational cost, the time and the total grid number.

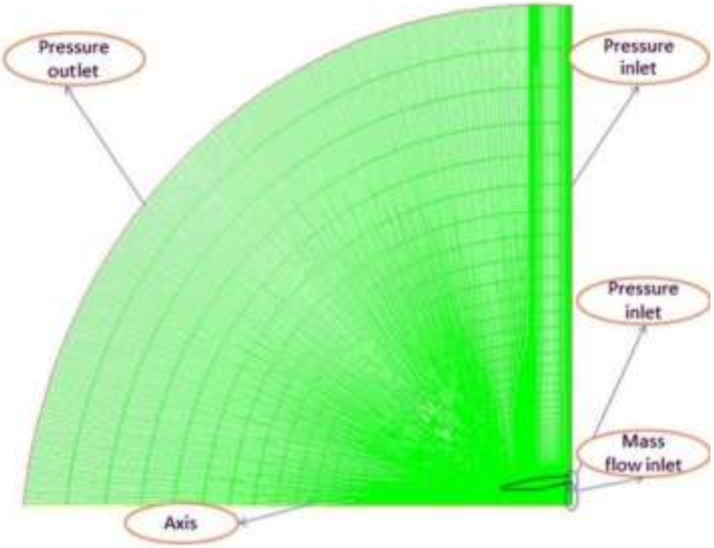

Fig.3 The scheme of boundary conditions.

2.1.1 Governing Equations

The used governing equations are as follows:

Mass conservation equation:

$$\frac{\partial \rho}{\partial t}+\frac{\partial}{\partial x}(\rho v_x)+\frac{\partial}{\partial r}(\rho v_r)+\frac{\rho v_r}{r}=0 \tag{1}$$

Momentum conservation equation:

$$\frac{\partial}{\partial t}(\rho v_x)+\frac{1}{r}\frac{\partial}{\partial x}(r\rho v_x v_x)+\frac{1}{r}\frac{\partial}{\partial r}(r\rho v_r v_x)=-\frac{\partial p}{\partial x}+\frac{1}{r}\frac{\partial}{\partial x}\left[r\mu\left(2\frac{\partial v_x}{\partial x}-\frac{2}{3}(\nabla.\mathbf{v})\right)\right]+\frac{1}{r}\frac{\partial}{\partial r}\left[r\mu\left(\frac{\partial v_x}{\partial r}+\frac{\partial v_r}{\partial x}\right)\right] \tag{2}$$

And

$$\frac{\partial}{\partial t}(\rho v_r)+\frac{1}{r}\frac{\partial}{\partial x}(r\rho v_x v_r)+\frac{1}{r}\frac{\partial}{\partial r}(r\rho v_r v_r)=-\frac{\partial p}{\partial r}+\frac{1}{r}\frac{\partial}{\partial x}[r\mu(\frac{\partial v_r}{\partial x}+\frac{\partial v_x}{\partial r})]+\frac{1}{r}\frac{\partial}{\partial r}[r\mu(2\frac{\partial v_r}{\partial r}-\frac{2}{3}(\nabla.\mathbf{v}))]-2\mu\frac{v_r}{r^2}+\frac{2}{3}\frac{\mu}{r}(\nabla.\mathbf{v}) \quad (3)$$

Where:

$$\mathbf{v}=\frac{\partial v_x}{\partial x}+\frac{\partial v_r}{\partial r}+\frac{v_r}{r}$$

(4) ∇.

Energy equation:

$$\frac{\partial}{\partial t}(\rho E)+\frac{\partial}{\partial x_j}[u_i(\rho E+p)=\frac{\partial}{\partial x_j}[(k_T+\frac{C_p\mu_t}{Pr_t})\frac{\partial T}{\partial x_j}+u_j(\tau_{ij})_{eff}] \quad (5)$$

2.2 Turbulence Model

Menter [26] created the Shear Stress Transport (SST) k-ω model, where the k-ω model was used in the near-wall region, and the k-ε model was used in the far-field, which was not influenced by the freestream. Menter's SST k-ω model offers a reasonable nozzle flow separation prediction, and various shocks happen because of under expansion and overexpansion. Transport equations for the SST k-ω model are given by:

$$\frac{\partial}{\partial t}(\rho k)+\frac{\partial}{\partial x_j}(\rho k u_i)=\frac{\partial}{\partial x_j}\left(\Gamma_k\frac{\partial k}{\partial x_j}\right)+G_k+Y_k \quad (6)$$

And [47, 48]:

$$\frac{\partial}{\partial t}(\rho\omega)+\frac{\partial}{\partial x_j}(\rho\omega u_i)=\frac{\partial}{\partial x_j}\left(\Gamma_\omega\frac{\partial \omega}{\partial x_j}\right)+G_\omega-Y_\omega+D_\omega \quad (7)$$

2.3 Grid Study

For the engine coolant mass flow rate, the grid number is gradually increased in six steps from 48100 to 311494 cells to ensure the least possible impact of grid size on the computational results. With a coarse grid, numerical calculations frequently produce unreliable results. In order to produce a specified mass flow rate of 0.34479920 at the inlet, the grid independence test was examined. The coolant flow rate in 311494 cells was unaffected by the mesh sizes, as indicated in Table 1. As previously stated, the grid was suitable in the computational domain to reduce the value of Y^+ near the walls to less than one because the k-ω SST turbulence model was used to simulate. The value of Y^+ close to the wall was around 90 prior to modifying the grid, which was inappropriate for the SST turbulence model. Due to the fact that Y^+ was close to 0.4, an attempt was made to lower its value to less than one after changing the computational grid. This number matched the SST turbulence models.

Table 1. Grid independence test (Rate of coolant flow with the number of cells).

Coolant flow rate	No of cells
0.34416248	48100
0.34455001	97500
0.34472451	155200
0.34477897	213600
0.34479225	285440

0.34479920	311494

2.4 Validation

The lift and the drag coefficients of the NACA0012 blade were numerically computed and compared with the available experimental findings since there were no experimental data from the mentioned aerial flying engine to validate the numerical method. Fig.4 shows the grid around the blade. 2D structured mesh was generated around the blade using the multi-block technique in Gambit. Moreover, it was obvious that a fine mesh was generated near the blade boundary in Fig.4.

In this step, the boundary conditions were utilized as follows (Fig.5):

- No-slip boundary conditions on blade walls.
- Inlet velocity boundary condition on other boundaries.

In the Fig.4 the computational domain with inlet velocity boundary conditions is demonstrated.

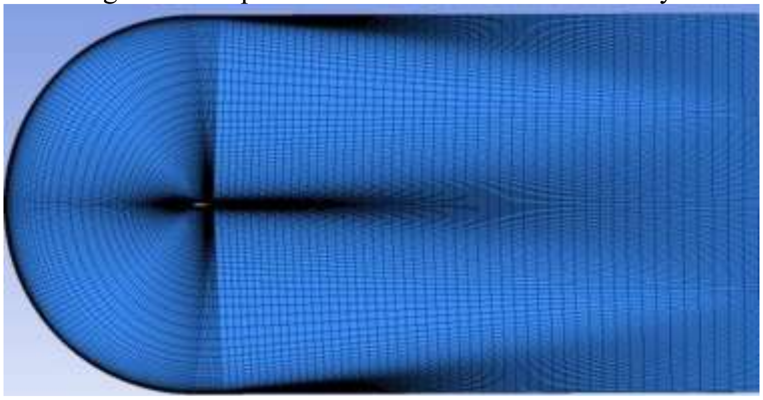

Fig.4 Computational grid around the NASA0012 blade.

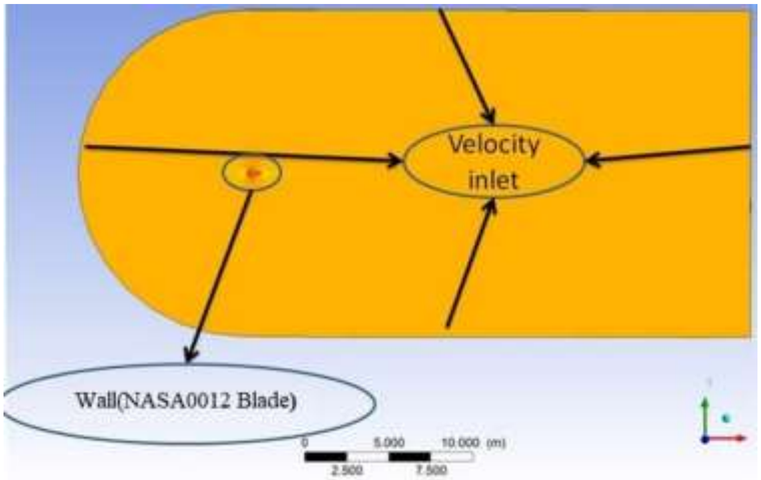

Fig.5 Boundary conditions

At a zero angle of attack, the Mach number contour around the blade is depicted in Fig. 6. There is no reverse flow at any location in the solution domain, and the Mach number contour is symmetrical around the blade. The streamlines around the blade are also shown in Fig. 7. Because of the blade's symmetry, as seen in Fig. 7, the streamlines are perfectly parallel at the blade's end. It indicates that the flow field is not deviating from normal in any way.

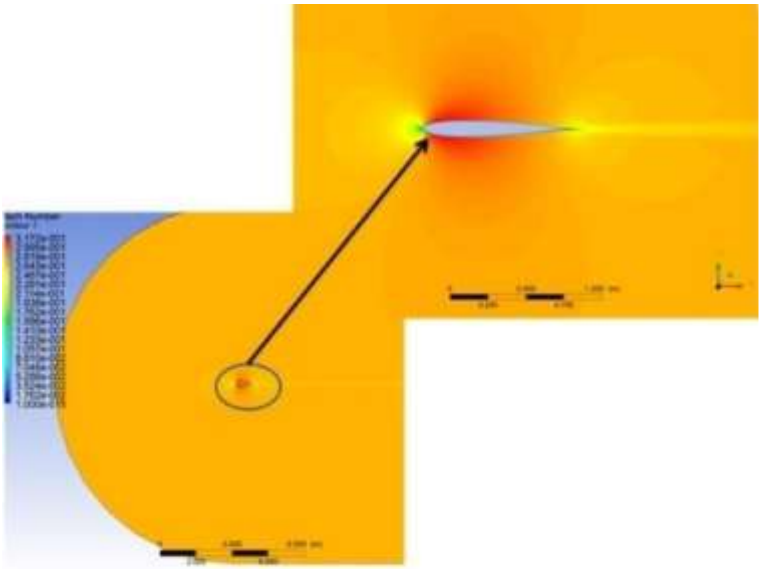

Fig.6 The Mach number contour in the computational domain and near the blade.

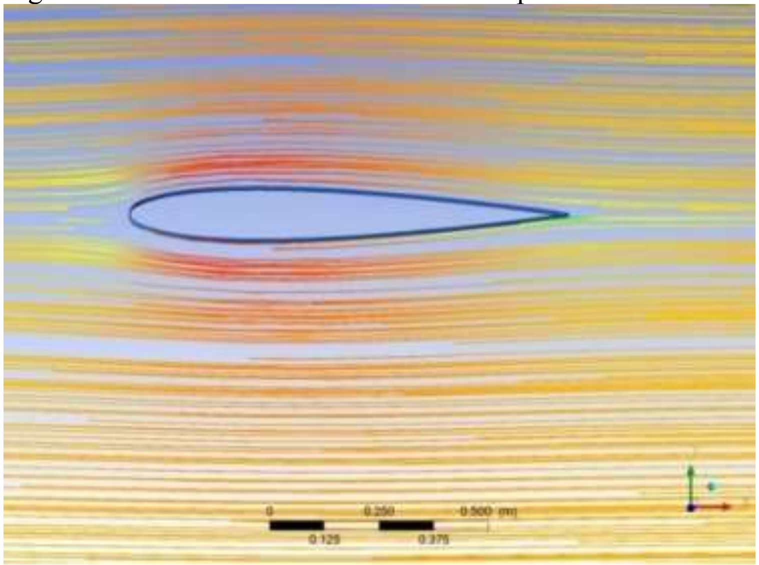

Fig.7 The streamlines near the blade.

The comparison of the available experimental and numerical results is shown in Fig. 8. The numerical and experimental results were in good agreement, as shown in Fig. 8. The largest mistake, with a value of roughly 4%, occurred at the angle of attack close to the stall.

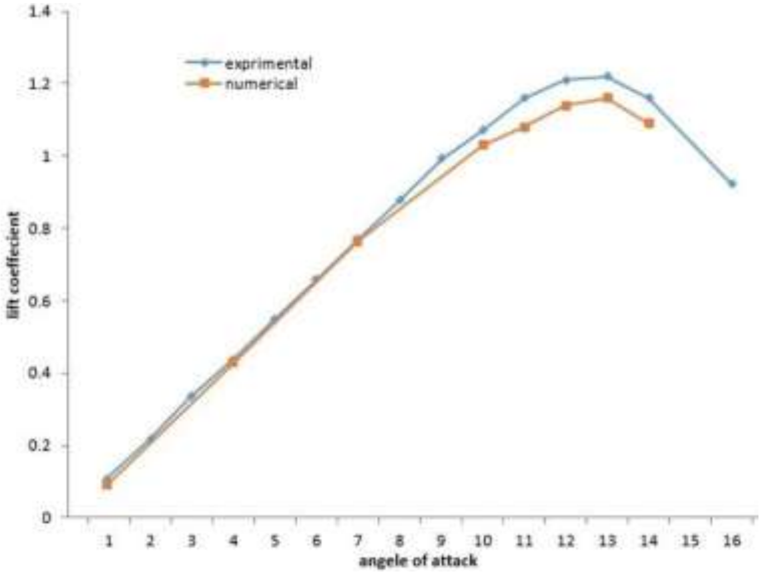

Fig.8 The comparison of lift coefficient between numerical analysis and experimental data.

Numerical Results and Discussions

In this section, several contours are presented so that the nozzle and nacelle are axially similar. Fig.9 depicts the velocity contour in the solution domain. In contours presented, coolant fluid Inlet Pressure is equal to 10,000 Pascal.

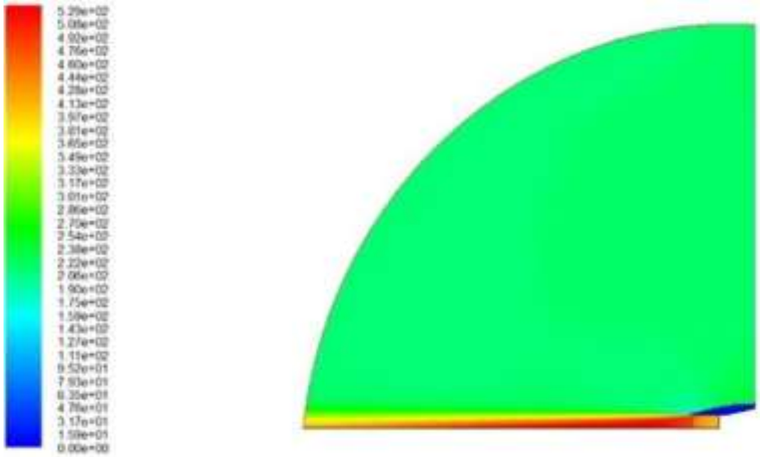

Fig.9 Velocity contour in the computational domain.

In Fig.10, pressure contour is exhibited in the solution domain. There is a negative pressure near the nozzle outlet, which causes the coolant fluid to suck and causes the coolant flow rate to be slightly higher.

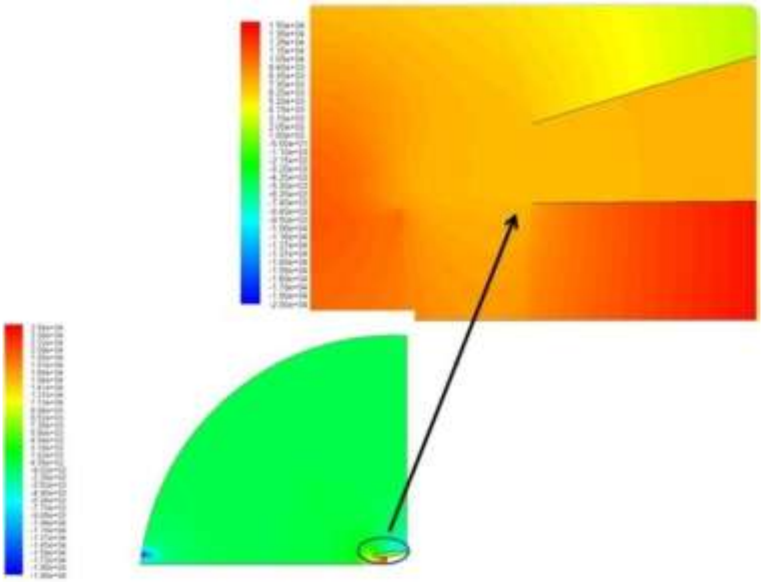

Fig.10 Static pressure contours in the computational domain.

Moreover, the static and total temperature contours are shown in Figs.11 and 12.

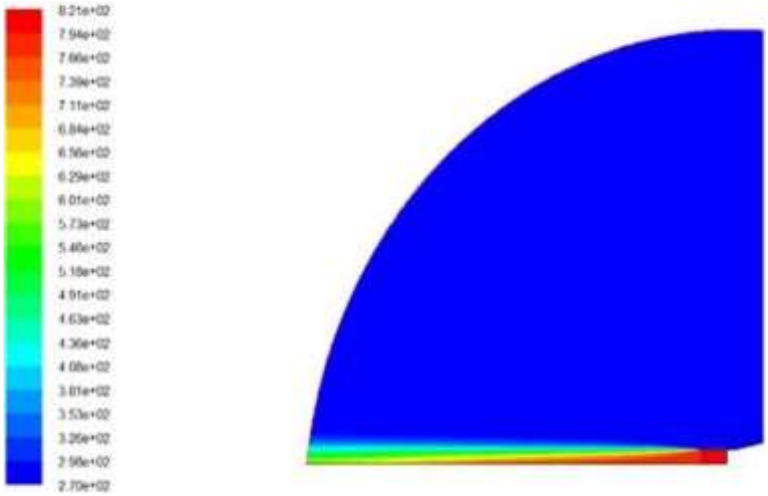

Fig.11 Static temperature contour in the computational domain.

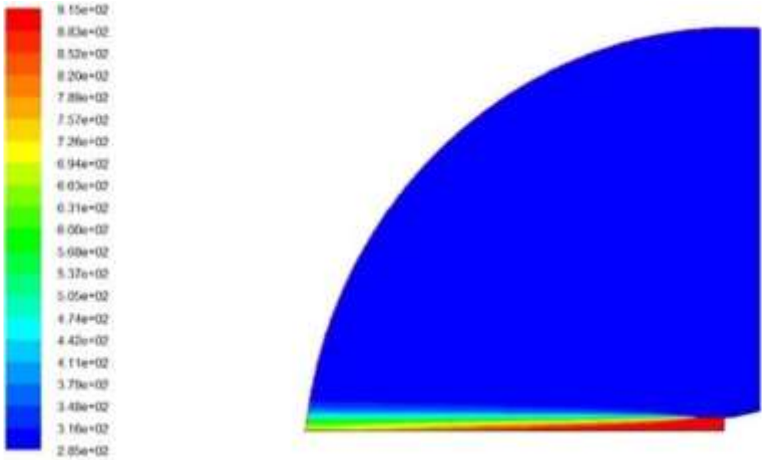

Fig.12 Total temperature contour in the computational domain.

The streamlines in the nozzle outlet are depicted in Fig.13. As revealed in Fig.13, the suction impact of the coolant fluid flow on the outlet jet is partly seen.

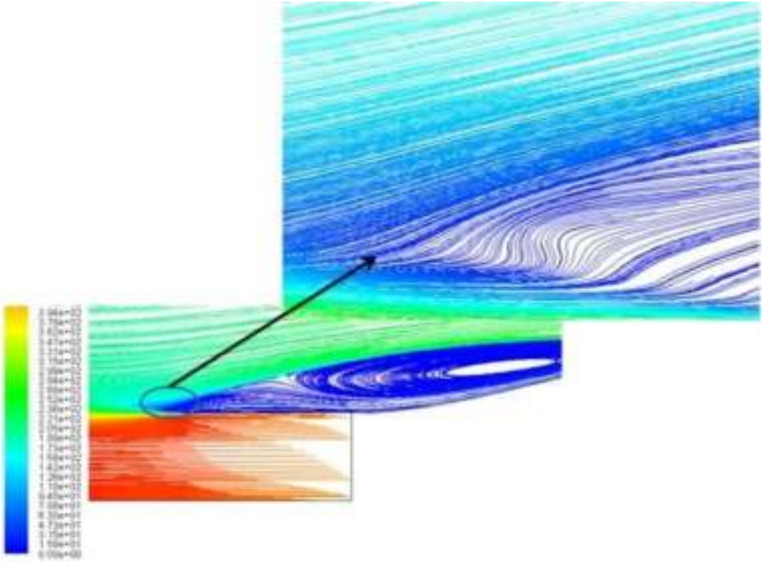

Fig.13 The streamlines near the nozzle wall.

3. Results and Discussion

3.1 The Effect of the Axial Distance between Nacelle and Nozzle on the Engine Performance In this section, by changing the nozzle axial distance from the nacelle, the optimal distance was computed to obtain the engine's maximum coolant fluid flow rate. Between 0 and 2.5 cm was selected as the axial distance between the nozzle and the nacelle. At intervals of 0 cm, 0.5 cm, 1.5 cm, and 2.5 cm, numerical analysis was performed. The pressure value spans from 1.1 to 1.3 bar in the numbers of 1.1, 1.15, 1.2, 1.25, and 1.3 bar to verify that the ideal distance was picked appropriately because there were no experimental data for engine cooling fluid pressure. From the nozzle to the engine's nacelle, Table 2 shows the value of coolant fluid mass flow rate in terms of axial distance and cooling fluid pressure.

Table 2. The coolant flow rate regarding coolant fluid pressure and axial nozzle distance from the nacelle.

	P=3 (bar)	P=2.5 (bar)	P=2 (bar)	P=1.5 (bar)	P=1 (bar)	The axial distance of nacelle to the nozzle
Coolant mass flow rate (Kg/s)	0.60070461	0.52841445	0.44596988	0.34742791	0.21673637	0
Coolant mass flow rate (Kg/s)	0.60013179	0.52774101	0.44515337	0.34638923	0.21505093	0.5
Coolant mass flow rate (Kg/s)	0.59951428	0.52699145	0.44422132	0.34509491	0.21271856	1.5
Coolant mass flow rate (Kg/s)	0.59543942	0.52359997	0.44178671	0.34416248	0.21452137	2.5

The results in Table 2 demonstrate that a distance between 0 and 0.5 is the ideal choice. However, as can be shown, the coolant fluid flow rate was not significantly affected by the distance between the nozzle and the nacelle. In other words, this shows that the suction rate caused by the outlet jet of hot fluid had very little effect on the cooling fluid flow rate when the axial distance was altered in the range specified (between 0 and 2.5 cm). The issue was numerically investigated to determine the impact of coolant mass flow in the engine and to explore the suction rate of the jet nozzle output on the coolant fluid flow rate. The effect of the nozzle's exit mass flow rate on the engine's coolant fluid mass flow rate is shown in Table 3.

Table 3 The impact of outlet mass flow rate of the nozzle on the mass flow rate of the engine cooling fluid.

Coolant mass flow rate(kg/s)	outlet mass flow rate of nozzle(kg/s)
0.34742791	7
0.34450494	6
0.34017925	5
0.34012727	4

The mass flow rate of the coolant fluid did not significantly change when the outlet mass flow rate of the nozzle was altered, as indicated in Table 3. According to this factor, the coolant fluid mass flow rate was mostly influenced by the cooling fluid pressure and was independent of the fluid jet at the nozzle's outlet (Hot fluid jet).

3.2 Impact of Nacelle Length on the Engine Performance

The effect of a longer nacelle on the engine's coolant mass flow rate will be covered in this section. The nacelle length was increased to 6.5 cm as a result of this investigation. This extension of the nacelle length was done at a fixed diameter. The flow grows towards the nozzle outlet as the fluid leaves it, which causes the flow in the area around it to suction. One of the elements affecting the far-field fluid flow around the nozzle was the flow rate of the cooling fluid.

On the other hand, this flow had high pressure that tended to go into the nacelle and the engine's nozzle. As a result, this factor reduced the coolant fluid flow rate. The vortex caused at the nozzle outlet was mixing the far-field fluid with the coolant fluid (Fig. 14). Enhancing the nacelle length caused the farfield flow not to prevent the flow from coming out of the nozzle (Fig.15). As the nacelle length enhanced, the coolant fluid flow rate remarkably enhanced. With a growth in the nacelle length, the coolant flow rate increased by about 52% at 1.5 bar inlet pressure. Finally, the coolant fluid flow rate value for various nozzle lengths is shown in Table 4.

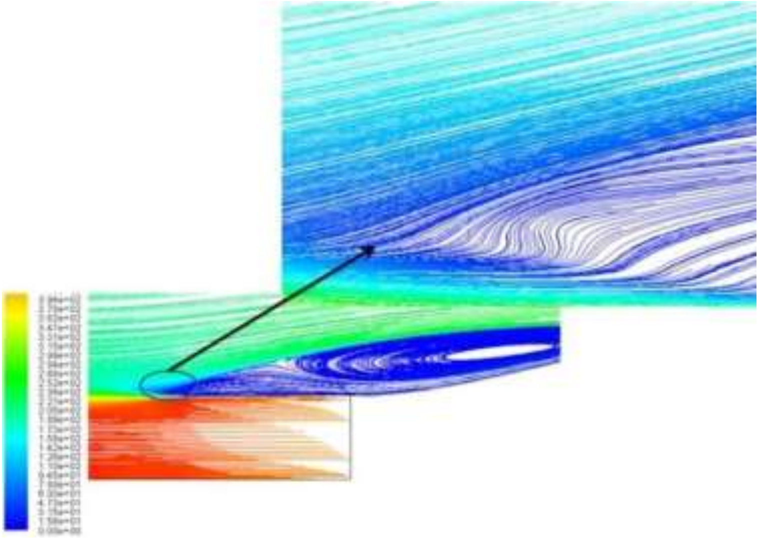

Fig.14 Streamlines in the nozzle region of the engine with initial nacelle length.

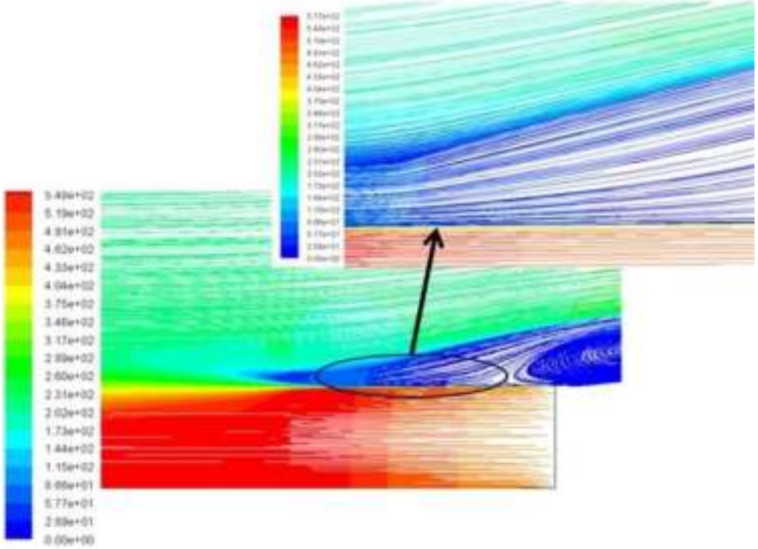

Fig.15 Streamlines in the nozzle zone of the engine with an increase in nacelle length.

Table 4 Coolant flow rate (nacelle length increased by 6.5cm).

	P=3 (bar)	P=2.5 (bar)	P=2 (bar)	P=1.5 (bar)	P=1 (bar)	The axial distance of nacelle to the nozzle

Coolant mass flow rate (Kg/s)	0.69738882	0.64376122	0.58656976	0.52456781	0.45556474	0
Coolant mass flow rate (Kg/s)	0.79460017	0.64376122	0.67265787	0.6102496	0.54554323	0.5
Coolant mass flow rate (Kg/s)	0.88217069	0.85756418	0.77970082	0.73630001	0.62554323	1.5
Coolant mass flow rate (Kg/s)	0.99117206	0.95665765	0.87811508	0.79735012	0.67420989	2.5

4. Conclusions

In this study, ANSYS Fluent was used to perform a 2D aerodynamic analysis. In order to accurately calculate the complex adverse pressure gradient flows, separation flows, and the closed equations system with the ideal gas equation of state, the two-equation Menter's Shear Stress Transport (SST k-ω) model was utilized as a turbulence model. This investigation sought to determine how the length of the nacelle and the axial distance between the nozzle and nacelle affected the performance of the aerial flying engine.

Because the k-ω SST turbulence model was used to simulate the results of this investigation, mesh generation in Gambit was carried out. The grid size in the computational domain had to be suitable to reduce the value of Y^+ close to the walls. Because of this, the Y^+ of the chosen grid size was lower than one. Since the numerical method needed experimental data from the aerial flying engine to be validated, the lift coefficient of the NACA0012 blade was computed numerically and compared to the results of the existing experiments. The results showed that changing the nozzle's outlet fluid flow rate had little effect on the coolant fluid flow rate. This result demonstrated that the coolant fluid mass flow rate was primarily influenced by the coolant fluid pressure and was independent of the nozzle outlet jet's suction rate (hot fluid jet).

However, the coolant flow rate was greatly enhanced by a longer nacelle on the engine. At the 1.5 bar inlet pressure in this case, the coolant flow rate rose by around 52%. Subsequently, the engine's nozzle was analyzed in three dimensions in detail to ensure the two-dimensional axisymmetric analysis. This means that the two-dimensional axisymmetric analysis had good solution accuracy in this study, and the two-dimensional assumption for the nozzle analysis was a very suitable one.

Statements and Declarations

The authors declare that they have no known competing financial interests or personal relationships that could have appeared to influence the work reported in this paper.

The authors have no conflicts of interest to declare. All co-authors have seen and agree with the contents of the manuscript and we certify that the submission is original work and is not under review at any other publication.

5. Reference

[1] Kosman, Wojciech, Andrzej Rusin, and Piotr Reichel. "Application of an energy storage system with molten salt to a steam turbine cycle to decrease the minimal acceptable load." Energy (2022): 126480. [2] Zhang, Guojie, et al. "Effect of NaCl presence caused by salting out on the heterogeneoushomogeneous coupling non-equilibrium condensation flow in a steam turbine cascade." Energy 263 (2023): 126074.

[3] Salvini, Coriolano, Ambra Giovannelli, and Hiyam Farhat. "On the possibility of using an industrial steam turbine as an air expander in a Compressed Air Energy Storage plant." Journal of Energy Storage 55 (2022): 105453.

[4] Li, Ai-Hong, et al. "Parametric optimization of steam turbine networks by using commercial simulation software." Chemical Engineering Research and Design 184 (2022): 246-255.

[5] Hu, Pengfei, et al. "Dynamic response of turbine blade considering a droplet-wall interaction in wet steam region." Energy 265 (2023): 126323.
[6] Krechkovska, H., et al. "Peculiarities of fatigue fracture of high-alloyed heat-resistant steel after its operation in steam turbine rotor blades." International Journal of Fatigue 167 (2023): 107341.
[7] Peymani, Alireza, et al. "Connection a vapor jet refrigeration system to a steam injected gas turbine." Energy 261 (2022): 125246.
[8] Lakzian, Esmail, Shima Yazdani, and Bok Jik Lee. "Passive control optimization of condensation flow in steam turbine blades." International Journal of Mechanical Sciences 237 (2023): 107804.
[9] Yu, Jianxi, et al. "Gross error detection in steam turbine measurements based on data reconciliation of inequality constraints." Energy 253 (2022): 124009.
[10] Han, Xu, et al. "Research on wet steam condensation flow characteristics of steam turbine last stage under zero output condition." International Journal of Thermal Sciences 179 (2022): 107691.
[11] Cao, Lihua, Xiaoli Li, and Di Wang. "Thermal system for comprehensive utilization of boiler and steam turbine energy of coal-fired power units based on the S-CO2 cycle." Energy Reports 8 (2022): 15286-15295.
[12] Azghadi, F. Ebrahimzadeh, et al. "Numerical simulation of nucleating flow and shock capturing in steam turbines by a simple low-dissipation upwind scheme using an Eulerian-Lagrangian model." Computers & Fluids 249 (2022): 105699.
[13] Ding, Hongbing, et al. "Unsteady non-equilibrium condensation flow of 3-D wet steam stage of steam turbine with roughness using sliding mesh method." International Journal of Thermal Sciences 179 (2022): 107674.
[14] Pashchenko, Dmitry, Ravil Mustafin, and Igor Karpilov. "Thermochemical recuperation by steam methane reforming as an efficient alternative to steam injection in the gas turbines." Energy 258 (2022): 124913.
[15] Cao, Lihua, Shuang Liu, and Rui Wang. "Influence of axial clearance on solid particle erosion and efficiency of governing stage in ultra-supercritical steam turbine based on rebound effect." Advanced Powder Technology 33.11 (2022): 103789.
[16] Xiong, Jiawang, et al. "The additional control strategies to improve primary frequency response for hybrid power plant with gas turbines and steam turbines." Energy Reports 8 (2022): 557-564.
[17] Ashraf, Waqar Muhammad, et al. "Artificial intelligence based operational strategy development and implementation for vibration reduction of a supercritical steam turbine shaft bearing." Alexandria Engineering Journal 61.3 (2022): 1864-1880.
[18] Mei, Ziyue, et al. "Sensitivity analysis of low-pressure gland seal deformation behavior during vacuuming for a 1000 MW nuclear steam turbine based on thermo-mechanical coupling method." Annals of Nuclear Energy 167 (2022): 108762.
[19] Kafaei, Amir, et al. "The best angle of hot steam injection holes in the 3D steam turbine blade cascade." International Journal of Thermal Sciences 173 (2022): 107387.
[20] Kartal, Furkan, and Uğur Özveren. "Investigation of an integrated circulating fluidized bed gasifier/steam turbine/proton exchange membrane (PEM) fuel cell system for torrefied biomass and modeling with artificial intelligence approach." Energy Conversion and Management 263 (2022): 115718. [21] ANSYS Inc, ANSYS-Fluent Documentation (ANSYS-Fluent Getting Started Guide, ANSYS-Fluent User's Guide, ANSYS Fluent Theory Guide, ANSYS-Fluent Tutorial Guide), Pennsylvania, USA, 2013. [22] Menter FR. Two-equation eddy-viscosity turbulence models for engineering applications, AIAAJ, 1994, 32(8), pp.1598–1605.
[23] Ahmadi M, Khosravi FA. CFD Simulation of Non-Newtonian Two-Phase Fluid Flow through a Channel with a Cavity, Thermal science, 2020, 24(2B), pp.1045-1054.
[24] Ahmadi M, Mirjalily SAA, Oloomi SAA. RANS K-ω Simulation of 2D Turbulent Natural Convection in an Enclosure with Heating Sources, IIUM Engineering Journal, 2019, 20 (1), pp.229–244. [25] Ahmadi M, Mirjalily SAA, Oloomi SAA. (2020) Simulation of Pollutant Dispersion in Urban Street Canyons Using Hybrid RANS-LES Method with Two-Phase Model. Computers and Fluids, 210: 104676.
[26] Menter FR. Two-equation eddy-viscosity turbulence models for engineering applications, AIAAJ, 1994, 32(8), pp.1598–1605.